

Monitoring the Dissolution Mechanisms of Amorphous Bicalutamide Solid Dispersions via Real-Time Raman Mapping

Francesco Tres,^{*,†} Jamie D. Patient,[†] Philip M. Williams,[†] Kevin Treacher,[‡] Jonathan Booth,[‡] Leslie P. Hughes,[‡] Stephen A. C. Wren,[‡] Jonathan W. Aylott,[†] and Jonathan C. Burley^{*,†}

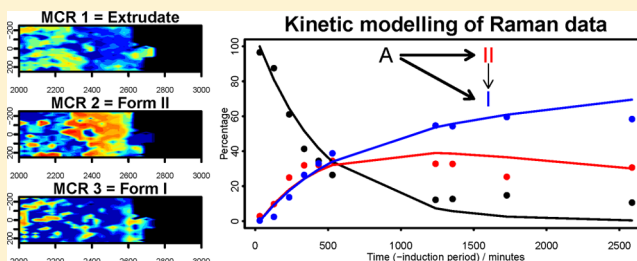
[†]School of Pharmacy, University of Nottingham, Boots Science Building, Nottingham NG7 2RD, United Kingdom

[‡]Pharmaceutical Development, AstraZeneca, Macclesfield SK10 2NA, United Kingdom

S Supporting Information

ABSTRACT: Real-time *in situ* Raman mapping has been employed to monitor, during dissolution, the crystallization transitions of amorphous bicalutamide formulated as a molecular dispersion in a copovidone VA64 matrix. The dissolution performance was also investigated using the rotating disc dissolution rate methodology, which allows simultaneous determination of the dissolution rate of both active ingredient and polymer. The dissolution behavior of two bicalutamide:copovidone VA64 dispersion formulations, containing 5% (w/w) and 50% (w/w) bicalutamide, respectively, was investigated, with the aim of exploring the effect of increasing the bicalutamide loading on the dissolution performance. Spatially time-resolved Raman maps generated using multivariate curve resolution indicated the simultaneous transformation of amorphous bicalutamide present in the 50% drug-loaded extrudate into metastable polymorphic form II and low-energy polymorphic form I. Fitting a kinetic model and spatially correlating the data extracted from the Raman maps also allowed us to understand the re-crystallization mechanisms by which the low-energy form I appears. Form I was shown to crystallize mainly directly from the amorphous solid dispersion, with crystallization from the metastable form II being a minor contribution.

KEYWORDS: bicalutamide, poorly soluble drugs, amorphous solid dispersions, dissolution, solid-state transformations, polymorphic changes, Raman mapping, multivariate curve resolution, kinetic modeling, spatial correlations



1. INTRODUCTION

An increasing number of drug candidates emerging from pharmaceutical development pipelines are characterized by poor dissolution and solubility profiles.¹ In light of this, there is a requirement for the pharmaceutical industry to develop innovative formulations to achieve the desired oral bioavailability and *in vivo* efficacy. A common strategy to improve the apparent solubility of poorly soluble drugs is to generate the amorphous form of the drug.^{2,3} Amorphous solids consist of disordered arrangements of molecules and do not possess a distinguishable crystal lattice. As a result, the dissolution rate of the amorphous form is higher than in its crystalline counterpart.⁴ However, the amorphous form is thermodynamically unstable and therefore tends to convert into the crystalline form over time, thereby compromising the drug bioavailability.^{5,6} An increasingly popular strategy to stabilize the amorphous state is the use of solid dispersions and solid solutions in which the drug is molecularly mixed with a water-soluble or water-swelling carrier, typically via hot melt extrusion or spray drying.^{7,8}

Although the physical stability of amorphous solid dispersion formulations has been widely probed, particularly focusing on the use of different polymers to inhibit drug re-crystallization,^{9,10} few studies have been conducted specifically to

understand their performance in a dynamic aqueous environment.^{11,12} Drug release from amorphous solid dispersions has been classified as polymer-controlled or drug-controlled, depending on the chemical nature of the components and on the carrier-to-drug ratio.¹³ Several processes have been demonstrated to be involved during the dissolution of amorphous solid dispersion formulations. The nucleation and crystallization of the drug either in the solid state or from a super-saturated state in solution, the generation of nano- and microparticles suspended in the dissolution medium, and the behavior of the carrier itself can significantly affect the overall dissolution performance.^{11,14–16} Due to the number of processes involved, the dissolution mechanisms of amorphous solid dispersions are extremely difficult to deconvolute.

Classical methods of investigating drug release, such as the use of USP dissolution apparatuses, involve dissolving a tablet in water or other biorelevant media and measuring the drug content in solution as a function of time using UV spectroscopy or HPLC.¹⁷ Data are not collected directly from the dosage

Received: December 12, 2014

Revised: March 31, 2015

Accepted: April 15, 2015

Published: April 15, 2015

form itself, and therefore solution-based methods do not offer any chemical or spatially resolved information on potential changes in the solid form during dissolution (e.g., recrystallization of the amorphous form, polymorphic transformations, or formation of hydrate states), which may be extremely important for developing reliable medicines with well-understood dissolution performance.

Given the limitations of classical solution-based methods, there have been a number of attempts to provide a full and clear picture of the drug release. Methods have included confocal fluorescence microscopy,¹⁸ mid-infrared (mid-IR),^{19,20} near-infrared (near-IR),^{21,22} and magnetic resonance imaging (MRI).^{23,24} The first three offer some chemical information, while MRI provides relatively low chemical specificity, but it is the only one of these methods that can provide three-dimensional information. Although near-IR and mid-IR are characterized by the highest chemical selectivity among the techniques mentioned ("multivariate data", one spectrum per pixel), their radiation is strongly absorbed by water molecules, which is not ideal for imaging in aqueous environments but can be worked around by integrating only bands for each component which appear distant from the absorption of water, as Kazarian et al. have shown.^{19,20,25}

Raman mapping has been demonstrated to be a useful tool to investigate the distribution of multiple components in solid dosage forms during dissolution.^{26,27} In a recent work, Strachan et al. employed coherent anti-Stokes Raman scattering (CARS) microscopy to image *in situ* the solid-state changes during dissolution in oral dosage forms containing theophylline anhydrate.²⁸ In CARS, compared to spontaneous Raman spectroscopy, two pulsed lasers are focused on the sample to generate a coherent anti-Stokes signal.²⁸ CARS requires very specialized equipment, while laboratory-based Raman requires only one laser and is therefore much more readily accessible. One of the key advantages of Raman spectroscopy is the access to the low-wavenumber region that has been demonstrated to be extremely sensitive to differences between amorphous and crystalline forms and among different polymorphic forms.^{12,29,30} In addition, Raman spectroscopy can, in principle, achieve a spatial resolution at the sub-micrometer level, while the maximum spatial resolution possible with the IR and near-IR radiations is diffraction-limited to 0.5 and 1–2 μm , respectively, although in practice it has been reported that the maximum spatial resolution for IR is 4 μm and that for near-IR is 6 μm .²⁶ In comparison to mid-IR and near-IR, Raman spectroscopy is relatively insensitive to water, offering therefore some potential advantages over the other state-of-the-art methods for investigating drug release from tablets in water.

Conventional Raman spectroscopic mapping was employed in the present work to deconvolute the dissolution mechanisms of bicalutamide:copovidone VA64 amorphous solid dispersions. Bicalutamide (Figure 1) is an important front-line treatment for prostate cancer. It is a non-steroidal anti-androgen that has an extremely low aqueous solubility (lower than 5 mg/L) and belongs to class II (low solubility, high intestinal permeability)

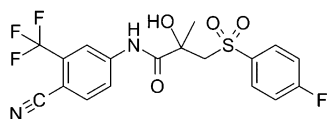


Figure 1. Molecular structure of bicalutamide.

of the biopharmaceutics classification system.^{31,32} Bicalutamide exists in two known crystalline phases (polymorphs I and II): form I is currently marketed, whereas form II is metastable and therefore can convert into form I in appropriate conditions.³³ The polymorphic forms of bicalutamide have been thoroughly characterized by Vega et al.,³⁴ who reported single-crystal X-ray structures and showed that low-energy form I relates monotropically to metastable form II; i.e., under standard conditions form I is more stable than form II at all temperatures. Due to the different crystal structures, forms I and II have different physicochemical properties. The melting points have been found by Vega et al. to be 192 °C for form I and 189 °C for form II, and form II has been demonstrated to be 2.4 times more water-soluble than form I at room temperature.³⁴ Researchers have also characterized forms I and II using Raman spectroscopy. They observed several differences between the two polymorphic forms in the fingerprint region because the two polymorphs contain different conformations of bicalutamide. Copovidone VA64 is a highly water-soluble polymer (solubility higher than 100 mg/L) that has been widely used to prepare single-phase amorphous solid dispersions of poorly soluble drugs.^{11,12,35}

The aim of the work presented below was to investigate the effects of increasing the amount of bicalutamide on the overall performance in water of the solid dispersion. For this reason, two bicalutamide:copovidone VA64 dispersions containing 5% (w/w) and 50% (w/w) bicalutamide were prepared. The rotating disc dissolution rate (RDDR) test, which is an extension of the standard intrinsic dissolution rate (IDR) test, was employed. The IDR test is an important biopharmaceutics screening tool to measure the dissolution rate normalized to the exposed surface area of a material.³⁶ Formally, IDR applies only to pure drug substances. By coupling an IDR apparatus to a HPLC system, the partial RDDR of both the drug substance and the excipients can be measured and compared for different formulations. The RDDR test has been recently demonstrated to be a useful tool for investigating the dissolution behavior of amorphous solid dispersions.¹² Real-time and *in situ* Raman mapping was also employed to monitor the solid-state transformations that occur during the dissolution of amorphous bicalutamide dispersions.

2. EXPERIMENTAL SECTION

2.1. Materials and Methods. Crystalline bicalutamide form I was provided by AstraZeneca (Macclesfield, United Kingdom). The polymorphic purity of form I was verified by Raman spectroscopy and XRPD. Copovidone (Kollidon VA64) was supplied by BASF (Ludwigshafen, Germany) and used as received, without any further purification.

2.2. Preparation of Amorphous Form and Crystalline Bicalutamide Form II. The amorphous form of bicalutamide was obtained by heating form I to 200 °C and quench-cooling the melt at room temperature. Raman spectroscopy and XRPD confirmed the formation of the amorphous form and the absence of crystalline material. Crystalline bicalutamide form II was produced according to patent, by heating the amorphous form to 175 °C.³⁷ Raman spectroscopy and XRPD confirmed the formation of polymorphic form II. Raman spectra and XRPD patterns from forms I and II and the amorphous form of bicalutamide are consistent with those previously reported by other workers.^{31–34}

2.3. Preparation of Bicalutamide:Copovidone Amorphous Solid Dispersions. A co-rotating twin-screw extruder

(Thermo Scientific HAAKE MiniLab II) was used to prepare the amorphous solid dispersions of bicalutamide and copovidone (5% and 50% w/w bicalutamide). Bicalutamide as received (form I) and copovidone were pre-mixed for 20 min in a Turbula T2F mixer (Willy A. Bachofen AG Mashinefabrik). The physical mixture was extruded at a temperature of 170 °C and a screw speed of 150 rpm. The materials were then cooled to room temperature and manually milled with a T&G CrushGrind mill to fine powders. Raman spectroscopy and XRPD confirmed the formation of the amorphous form and the absence of crystalline material.

2.4. X-ray Powder Diffraction (XRPD). XRPD patterns were obtained using a PANalytical CubiX PRO diffractometer ($\lambda = 1.5418 \text{ \AA}$). Samples were spun at 30 rpm and measured over the scan range from 2° to $40^\circ 2\theta$, with a 25 s exposure per $0.02^\circ 2\theta$ increment. The X-rays were generated by a copper long-fine focus tube operated at a voltage of 45 kV and a current of 40 mA.

2.5. Rotating Disc Dissolution Rate (RDDR) Measurements. RDDR were determined using the “Woods apparatus” rotating disc system. The die cavity has a diameter of 8 mm with an exposed surface area of 0.5 cm^2 . Testing was carried out in a Sotax AT7 semi-automated dissolution bath. About 250 mg of each sample was compressed under a force of ca. 20 kN for 1 min using a Specac manual hydraulic press. Compressed discs were immersed in 500 mL of dissolution medium (pH 6.8 blank fasted state simulated intestinal fluid) at $37^\circ \text{C} (\pm 0.5)$, and the rotational speed was set to 100 rpm. Samples were taken manually at regular time intervals over 120 min and then analyzed by reverse-phase high-performance liquid chromatography (RP-HPLC). All experiments were carried out in duplicate. All HPLC measurements were carried out on an HP Agilent 1100 instrument, equipped with an Agilent PLRP-S 300 $\text{\AA}/3 \text{ }\mu\text{m}/50 \text{ mm}$ column (polystyrene/divinylbenzene stationary phase). The flow rate was 1 mL/min, the column temperature was 40°C , and the UV detection wavelength was set to 210 nm. A linear gradient elution was used starting at 40% acetonitrile/60% deionized water and ending at 70% acetonitrile/30% deionized water after 2 min, with chromatograms collected for 3.5 min. A series of standard solutions were prepared in the relevant medium to generate a standard curve covering the concentration range of the dissolved sample. For each experiment, standards were analyzed alongside the RDDR samples. The partial RDDR of both drug and polymer was calculated using linear regression analysis. The partial RDDR of the material was obtained from the slope of the regression line. For the 5% extrudate RDDR was calculated using the first 20 min time period, where the trend is linear. For the 50% extrudate RDDR was obtained using the time interval between 40 and 120 min, where the trend of both bicalutamide and copovidone is linear, in accordance with Pharmacopoeia procedures.^{36,38}

2.6. Raman Spectroscopic Mapping. The dissolution performance of compressed extrudate powders was investigated. Circular compacts with a diameter of 5 mm and a weight of 50 mg were prepared with a Specac manual hydraulic press using a force of ca. 20 kN. The dissolution test was carried out using a flow cell previously described by Tres et al.¹² Deionized water was used as dissolution medium with the flow rate set to 5 mL/min. Data were acquired as a function of time using a HORIBA Jobin Yvon LabRAM HR confocal microscope/spectrometer. The system is equipped with an automated xyz stage (Märzhäuser) to allow mapping. All

samples were illuminated with a near-IR (785 nm) laser. Spectra were collected using a 50 \times objective (Olympus BX51) and a 300 μm confocal pinhole. All experiments used a 600 lines/mm rotatable diffraction grating along a path length of 800 mm to simultaneously scan a range of frequencies, and the spectra were detected using a SYNAPSE CCD detector (1024 pixels). The system was calibrated before collecting spectra with the Rayleigh line at 0 cm^{-1} , as well as using a standard silicon band at 520.7 cm^{-1} . For the raw materials, spectra were acquired in the wavenumber range from 30 to 4000 cm^{-1} , with the lower limit corresponding to the cutoff of the Rayleigh rejection filter. During the dissolution tests, prior to each map being collected, the z-axis position of the sample (i.e., level of sample perpendicular to optical axis) was adjusted to maximize the Raman signal. The time frames, dimensions of the mapped areas, and acquisition times for the 5% and 50% experiments are depicted in Table 1.

Table 1. Experimental Details for Raman Map Acquisition during the Dissolution Experiments of the 5% and 50% Extrudates

	5% extrudate	50% extrudate
time frame, minutes	80	2946
total no. of maps	7	14
total no. of spectra per map	121	1156
acquisition time per spectrum, seconds	2	2
acquisition time per map, minutes	8	90
mapped area, μm	500×500	500×1000
grid spacing x-axis, μm	50	15
grid spacing y-axis, μm	50	30

For Raman data analysis two approaches were adopted. First, to rapidly evaluate any spectral changes occurring during the dissolution tests, all the spectra from each map were integrated to generate a single averaged spectrum corresponding to each time point. Second, to obtain spatial information for the 50% extrudate compact dissolution experiment, false color maps were generated using multivariate curve resolution (MCR). In order to monitor changes as a function of both time and xy-position, a single data matrix was generated which includes all the spectra collected across the entire dissolution experiment time scale (16 184 spectra). Statistical analyses were performed using R software, which is open-source and well-documented software for statistical computing and graphics.³⁹ For MCR, the separate alternating least-squares algorithm (ALS)-MCR library was employed, with raw data being scaled prior to analysis using variance-scaling and mean-centering standard methods. All the raw data along with the numerical routines written in the R language are included in the Supporting Information for reference. An interested reader should therefore be able to reproduce all the data analysis presented in this paper.

2.7. Optical Imaging. A CoolSNAP-Pro CF camera (Media Cybernetics) equipped with a Nikon AF Micro NIKKOR 60 mm lens was employed to collect the photographic images during the dissolution of the extrudate formulations. The same flow cell experimental conditions previously described for the dissolution tests using Raman mapping were employed. For the dissolution test of the 50% extrudate, the “imgThreshold” function part of “biOps” package in R was employed to count the number of pixels above a pre-defined color threshold of the images collected during the

dissolution experiment. This allowed us to focus only on the pixels of the compact and build a trend which shows how the surface area of the compact changes as a function of time. An example of a thresholded image can be seen in Figure S1 in the Supporting Information.

3. RESULTS AND DISCUSSION

3.1. Optical Imaging and Rotating Disc Dissolution Rate. Before commencing a full discussion of the results, a key point needs to be made. Extrinsic factors such as hydrodynamics (e.g., disc rotation speed and fluid flow) and test conditions (e.g., temperature and pH of the medium) certainly differ between the RDDR test and Raman/optical imaging experiments. The primary aim of the present work is simply to investigate whether or not the combination of these techniques can provide a full and clear understanding of the bicalutamide release from solid dispersions.

Figure 2 shows the optical images observed during the dissolution under flow of the 5% and 50% drug-loaded

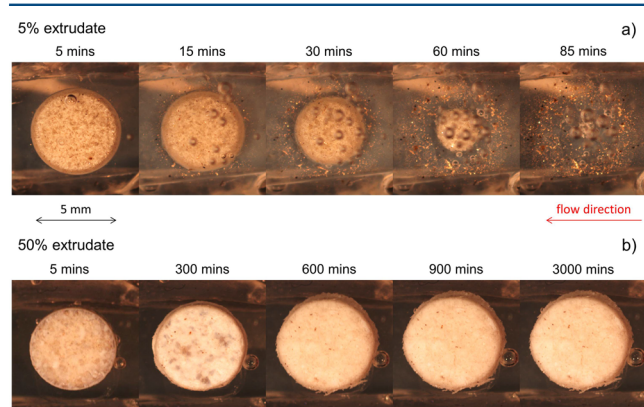


Figure 2. Optical images collected through the dissolution experiment for the 5% (a) and 50% (b) extrudate formulations.

extrudates. It is important to note the different time scales between the two experiments which is due to the difference in dissolution rates. The 5% extrudate formulation was completely dissolved after approximately 85 min, whereas the 50% drug-loaded extrudate remained intact after 3000 min. The optical imaging experiment does not provide any chemical information, but clearly shows that the two different drug loadings behave very differently in aqueous media. The 5% extrudate compact undergoes erosion and is completely dissolved by 85 min from the beginning of the experiment. The 50% extrudate compact swells during the first 600 min of the dissolution experiment and remains intact even after 3000 min. The initial swelling is confirmed by the kinetic trend generated by plotting the surface area of the compact vs time (Supporting Information, Figure S2). The swelling of a high drug-loaded extrudate has been

previously observed for amorphous solid dispersions of felodipine and copovidone.^{11,12}

RDDR measurements were then carried out in order to determine the amount of drug and polymer released into solution as a function of time. The RDDR method, as described previously,¹² uses HPLC to separate the active ingredient from the polymer and track the dissolution trend of both entities. The dissolution profile of the polymeric carrier provides valuable information in the case of binary systems, as the carrier can significantly affect the dissolution performance of the poorly soluble active ingredient.^{2,3} The dissolution rate of the polymer allows us to calculate an index of performance for the formulation, which illustrates how the drug and the polymer behave during the course of the dissolution experiment. The index of performance was defined by dividing the partial RDDR of bicalutamide by the total RDDR of the formulation (bicalutamide and copovidone) and then normalizing by the bicalutamide mass fraction. The equation to calculate the index of performance is reported in Table 2, along with the RDDR values for both 5% and 50% extrudates. Dissolution trends of the extrudates and pure crystalline form of bicalutamide are presented in the Supporting Information (Figures S3 and S4).

For the 5% extrudate, the partial RDDR value for bicalutamide is 0.24 mg/(min·cm²), and that for copovidone is 4.85 mg/(min·cm²). Compared to the IDR of pure crystalline bicalutamide (0.003 mg/(min·cm²), Figure S3), bicalutamide present in the 5% extrudate shows an 80-fold increase in dissolution rate. The index of performance results in a value close to unity, indicating that the two components have very similar dissolution trends and thus they dissolve simultaneously from the molecular dispersion. Given the low water solubility of bicalutamide, the overall behavior of the 5% bicalutamide-loaded solid dispersion is clearly dominated by water-soluble copovidone. Considering the 50% extrudate formulation, it is immediately apparent that the partial RDDR values of both bicalutamide and copovidone are much lower than those observed for the 5% extrudate. The partial RDDR of bicalutamide (0.008 mg/(min·cm²)) is comparable with the IDR of pure crystalline bicalutamide (0.003 mg/(min·cm²)). Optical images and RDDR data therefore suggest that the dissolution behavior of the 50% extrudate is dominated by the physicochemical properties of bicalutamide. The low water solubility and high hydrophobicity of the drug prevents the wetting and water uptake of the compact due to an insufficient ratio of copovidone to bicalutamide at the diffusion layer.³² As a result, the dissolution of both bicalutamide and copovidone is very limited.

Summarizing, the overall dissolution performance of the 5% drug-loaded extrudate is clearly polymer-dependent, with bicalutamide dissolving simultaneously with the hydrophilic polymer. For the 50% extrudate, optical images and RDDR measurements indicate that the behavior in water of the amorphous solid dispersion is dependent on the physicochem-

Table 2. Partial RDDR Values along with the Index of Performance for 5% and 50% Extrudates

drug loading	RDDR, mg/(min·cm ²)			index of performance ^a
	bicalutamide	copovidone	total	
5%	0.24(±0.005)	4.85(±0.127)	5.09(±0.127)	0.94(±0.030)
50%	0.008(±0.001)	0.025(±0.001)	0.033(±0.001)	0.48(±0.064)

^aThe index of performance was calculated by dividing the partial RDDR of bicalutamide by the total RDDR (bicalutamide plus copovidone) and then normalizing by the bicalutamide mass fraction: index of performance = (partial RDDR bicalutamide/total RDDR)/drug mass fraction.

ical properties of the hydrophobic bicalutamide. However, this does not clearly explain which processes occur during the course of the dissolution test, as data are not being collected directly from the dosage form, nor do the RDDR data provide any direct chemical explanation of the differences in dissolution rates between the 5% and 50% compacts. For this reason, real-time *in situ* Raman spectroscopic mapping along with off-line XRPD were used to investigate the samples.

3.2. Raman Spectroscopy. **3.2.1. Raman Spectra of “Dry” Raw Materials.** Raman spectra of the dry raw materials are available in Figure 3. The three solid forms of bicalutamide

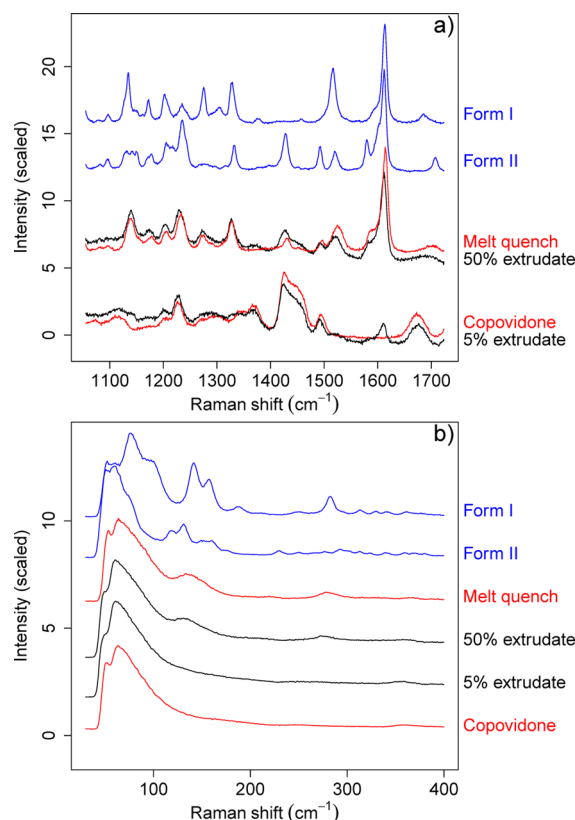


Figure 3. The 1055–1724 cm^{-1} (a) and 40–400 cm^{-1} (b) regions of the Raman spectra of “dry” raw materials. Data were variance-scaled and mean-centered before plotting. Y-offsets have been applied for presentation purpose and differ between the two panels.

present spectra with clear and obvious differences. Considering the region between 1055 and 1724 cm^{-1} (Figure 3a), the differences between the crystalline forms are reasonable, given that they are known to be conformational polymorphs. The band deriving from the stretching mode of the carbonyl group moves to higher wavenumber in form II (1709 cm^{-1}) compared to form I (1686 cm^{-1}). Due to the different conformation of forms I and II, the oxygen of the carbonyl group is involved in different intramolecular hydrogen bond interactions, which lead to the observed peak shift. Atoms are also involved in intermolecular interactions. The hydrogen bonding between the N–H of the amide group and one of the oxygen atoms of the sulfonyl group determines the formation of a dimer in the molecules of form II. This interaction would explain why an intense single band at 1517 cm^{-1} corresponding to the N–H bending and C–N stretching modes of the amide group is replaced by three peaks with inferior intensity appearing at 1428, 1493, and 1520 cm^{-1} in form II. In

addition, the particular conformation of form II enables π – π stacking interactions between the two rings. Due to this extra interaction form II presents a small peak at 1579 cm^{-1} (ring stretching mode) which is not present in the spectrum of form I. The schematic of the structural conformations of forms I and II is shown in the Supporting Information (Figure S5).

The amorphous (melt quench) form presents a spectrum more similar to that of crystalline form II than form I (e.g., bands at 1428 and 1493 cm^{-1} are present in the amorphous spectrum and the form II spectrum but not in the form I spectrum). This spectral similarity with form II suggests that the molecular conformation of the amorphous form is more similar to that of the metastable form II than that of highly stable form I. The amorphous form also exhibits greater peak widths than for the crystalline forms I and II, which is expected due to the molecular disorder inherent in the amorphous form but not present in the two crystalline forms. The spectra for the two extrudates are at first approximation simply a linear combination of the spectra for the amorphous drug and the polymer. A detailed inspection reveals some subtle differences, including a shift of the bands of the N–H bending mode at 1490 and 1516 cm^{-1} for the 50% extrudate, and at 1490 cm^{-1} for the 5% extrudate. These likely arise from the intermolecular hydrogen-bonding interactions between the amide of bicalutamide (N–H, proton donor) and the oxygen atoms of the carbonyl groups of copovidone (proton acceptor).³²

In the low-wavenumber region between 40 and 400 cm^{-1} (Figure 3b), the two crystalline forms of bicalutamide present clear, well-resolved bands, and the spectra are easily distinguishable from each other. This is wholly consistent with previous work by ourselves and other workers on low-wavenumber Raman spectroscopy applied to polymorphs.^{29,30} The melt-quenched bicalutamide, the two extrudates, and the pure polymer exhibit the typical broad boson peak at low wavenumber expected for amorphous materials,^{29,30} with the differences between these amorphous forms being subtle in this spectral region.

In summary, the various pure forms of bicalutamide and the extrudates can be distinguished using the reference Raman spectra, especially the region from 1055 to 1724 cm^{-1} . The low-wavenumber data (40–400 cm^{-1}) allow the crystalline forms to be distinguished both from each other and from the various amorphous forms. Bicalutamide form II and the amorphous form present similar spectra in the region between 1055 and 1724 cm^{-1} , and all amorphous forms (pure bicalutamide and the extrudates) exhibit similar spectra at low wavenumber.

3.2.2. Raman Spectroscopic Mapping. In order to gain good chemical and spatial detail on the dissolution processes in the compacts, Raman mapping was undertaken as a function of time in the region between 1055 and 1724 cm^{-1} . The data for the 5% extrudate are presented in the Supporting Information (Figure S6). No changes were observed during the dissolution beyond a reduction in the overall Raman intensity, which may result from the presence of the medium, loss of focus, and the surface changing from flat and even to relatively rounded and uneven as the dissolution proceeds. These factors will reduce the amount of sample in the Raman confocal plane and lead to a reduction in signal.

For the 50% compact, analysis indicated that significant changes occurred in the Raman spectra as the dissolution progressed. A univariate analysis (e.g., one peak intensity) is difficult due to the similarity in the bicalutamide spectra already noted between forms II and the amorphous form, as well as due

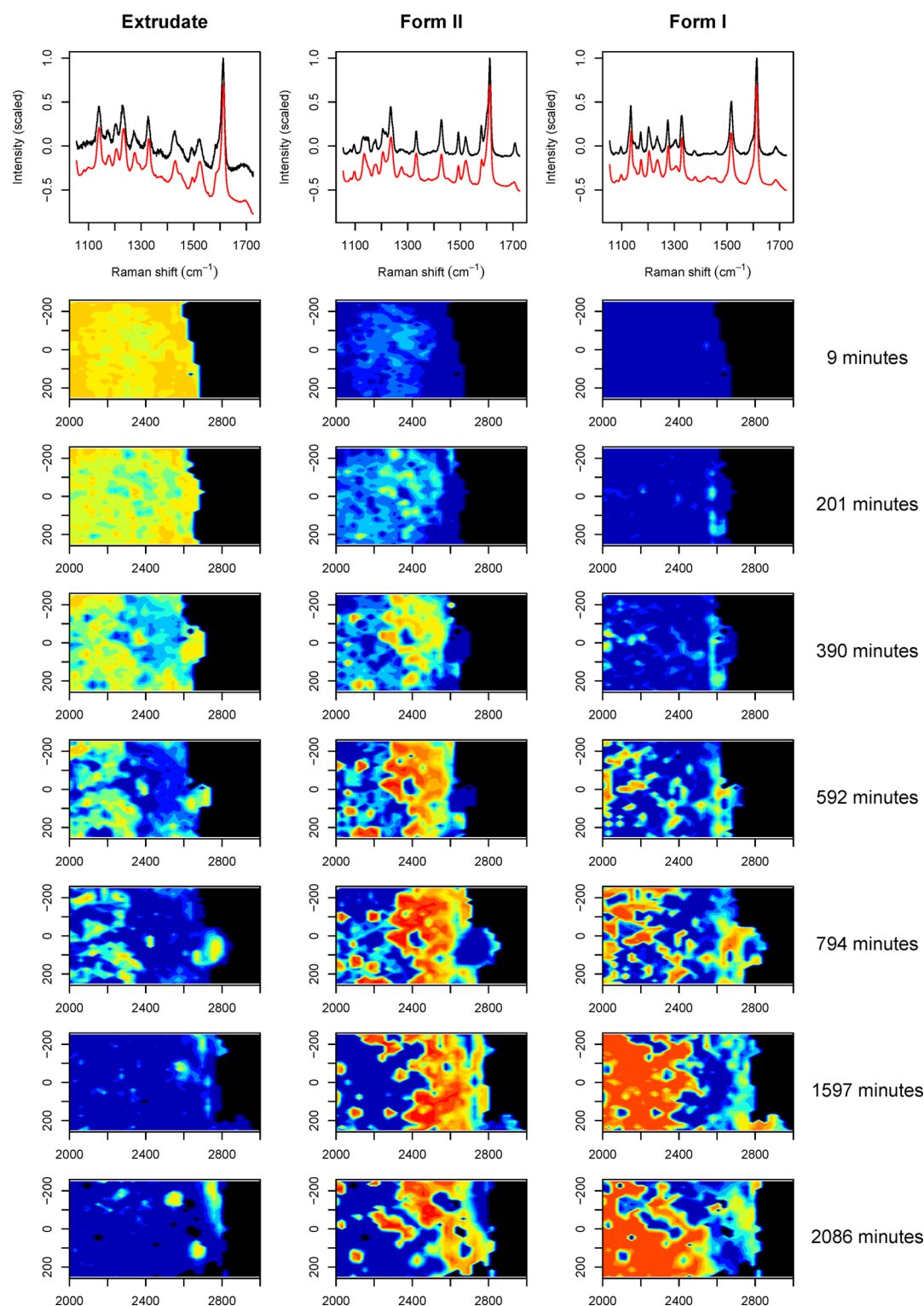


Figure 4. MCR Raman maps collected as a function of time through the dissolution experiment for the 50% extrudate formulation. Here presented are the loadings (with reference spectra in black) and the scores plots for the first three MCR components. White/red colors indicate areas where a particular phase is present to its maximum, while black/blue colors represent areas where it is present at its minimum. Areas with variable weighting of that phase are indicated by a continuum of white-red-orange-yellow-cyan-blue-black colors. Raw data were variance-scaled and mean-centered before MCR analysis was performed.

to the multicomponent nature of the formulation. To spatially and spectrally deconvolute the changes in the patterns for the 50% compact, we therefore employed MCR, which is a very well-established component analysis method and has been employed to resolve ToF-SIMS, IR, near-IR, and Raman data

from pharmaceutical samples.^{40–43} MCR requires input of a body of spectral data in a matrix format, each spectrum being tagged with a set of labels (e.g., x,y position), which is resolved by the MCR method into a number of components. The only user input is the requested number of components; i.e., MCR is

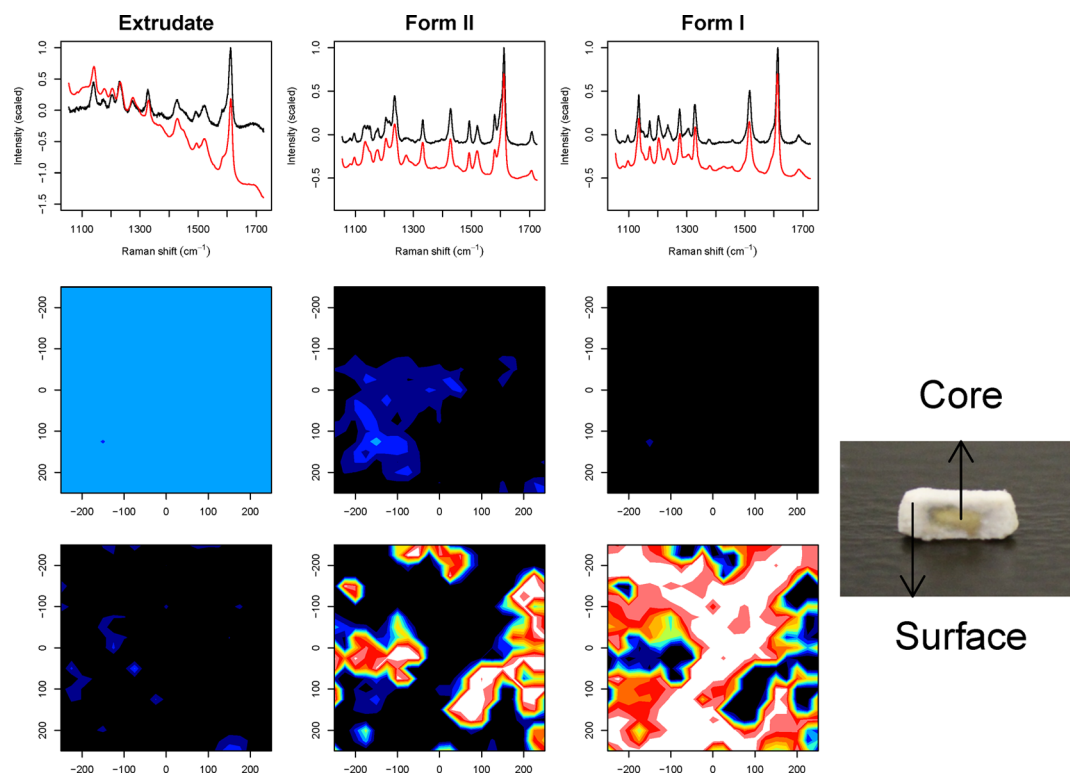


Figure 5. MCR Raman maps of the inner and outer sections of the compact. Here presented are the loadings (with reference spectra in black) and the scores plots of the first three MCR components, with data being variance-scaled and mean-centered prior to plotting.

a model-free method. Outputs from MCR include loadings (which in the present case correspond to Raman spectra of the resolved components) and scores (which provide the spectral weighting of a given component for the relevant unique set of labels). Labels typically comprise x and y positions, but there is no reason why they cannot include more information. To include time in our analysis, we simply concatenated all xy spectral maps together and included a time label for each input spectrum, in addition to the usual x and y labels. Our MCR results are reproducible for multiple runs, despite a different randomly generated set of numbers being employed as a starting model for each run. This provides confidence that our results are robust, which is important in the context of the well-known rotational ambiguities present in the MCR methodology.^{44,45} In our analysis, trial runs indicated that a suitable choice for number of components was three, and intensity thresholding was employed so that only the spectra from the compact were included in the analysis; i.e., the surrounding solution was excluded.

The results of our MCR analysis are presented graphically in Figure 4. Note that half the maps are shown for reasons of space, i.e., every second one starting at 9 min; however, the analysis included all maps, and the remaining time-point maps can be found in Supporting Information (Figure S7). Comparison of MCR loadings with reference spectra clearly indicates that the data have been resolved into components which correspond remarkably well with crystalline bicalutamide forms I and II, and the bicalutamide:copovidone extrudate. The variation in the scores as a function of space (within each map) and time (between maps, vertically descending) indicates that the starting material—the extrudate—decreases in weighting as time passes. In the early stages of the experiment, crystalline form II appears and grows in weighting, while after

approximately the 592 min time point the weighting of form I increases. Form I continues to increase in weighting at the expense of both the extrudate and form II, with the latter reducing in weighting after 889 min. The crystallization of amorphous bicalutamide into form II has been reported previously,^{33,34} and the hypothetical sequence amorphous \rightarrow metastable form II \rightarrow stable form I is in accord with the long-standing Ostwald's rule of stages. We note, however, that the results presented so far do not allow us to distinguish between the linear pathway amorphous \rightarrow form II \rightarrow form I and an alternative parallel pathway whereby amorphous \rightarrow form II and amorphous \rightarrow form I occur independently, with the crystallization to form I having a longer induction period than the crystallization to form II.

At the end of the experiment, the remaining compact was removed from the flow cell, cut through the center, and analyzed by Raman spectroscopy and visually. Data are presented in Figure 5. The recrystallization of the drug to a mixture of forms I (dominant at the end of the experiment) and form II occurs from the outside of the compact, with the interior being unchanged bicalutamide:copovidone extrudate. XRPD data from a powdered compact (Supporting Information, Figure S8) are in full accord with these *ex situ* Raman data.

The Raman mapping results, for the 50% extrudate, considered alongside the RDDR analysis, clearly indicate the hydrophilic polymer preferentially dissolves from the exterior of the compact. This leaves a drug-rich (therefore hydrophobic) shell on the outside of the compact, which is initially amorphous. The decrease in polymer concentration and increase in (amorphous) drug naturally leads to a crystallization of the drug. To address directly the question of the crystallization mechanism, we undertook a kinetic analysis of the crystallization processes, which we now outline.

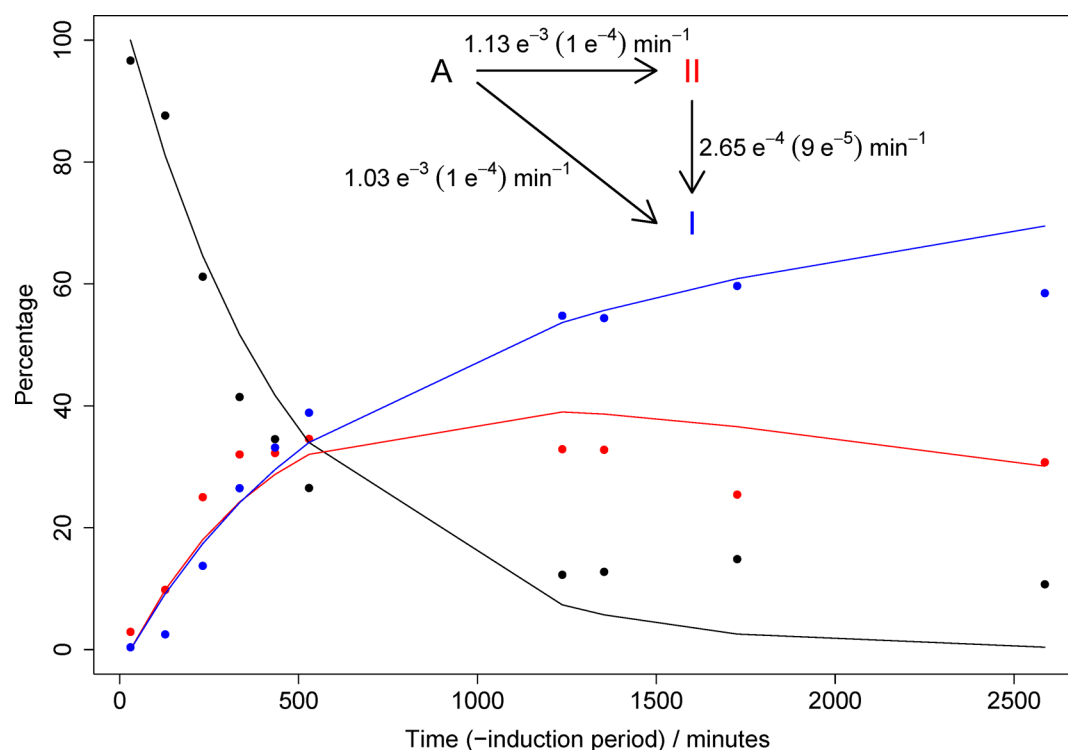


Figure 6. Experimental (dotted plots) and fitted (line plots) data of the three-step kinetic model. The induction period represents the first 360 min of the experiment. Estimated uncertainties are shown in parentheses.

While the MCR results are very useful for gaining a qualitative understanding of the spectral changes occurring, they are less useful for a quantitative analysis as the proportion of the spectral weighting cannot be related to the actual concentration without suitable standards. We therefore undertook a simple three-level classification procedure and assigned each spectrum at every xy time point to extrudate, form I, or form II, based upon the calculated correlations between the three reference spectra and the relevant experimental spectrum with its unique xy time labels. To remove the effect of the compact expanding/moving, the results are reported as percentages. Only the area corresponding to the compact was included in this analysis.

Results for the kinetic analysis are presented in Figure 6 both for the classification (i.e., experimental data) and for the kinetic model. The kinetic model included first-order rate constants for the processes $A \rightarrow II$, $A \rightarrow I$, and $II \rightarrow I$, which were adjusted according to the least-squares method until an optimized model was arrived at. To summarize, the rates of conversion $A \rightarrow II$ and $A \rightarrow I$ are similar, both being around 10^{-3} min^{-1} . The rate of conversion $II \rightarrow I$ is found to be approximately an order of magnitude lower, and therefore the analysis distinctly points toward a mixed crystallization mechanism. The appearance of form I directly from the amorphous form is favored compared to the conversion $II \rightarrow I$. The robustness of the analysis was cross-checked by constraining the rate constant for $A \rightarrow I$ to be 0 min^{-1} , and the resulting model (Figure S9) is clearly far inferior to the unconstrained model in which the rate constant for $A \rightarrow I$ is found to be of order 10^{-3} min^{-1} . We can therefore conclude that the parallel crystallization mechanism is dominant compared to the serial one in terms of kinetics.

Spatial correlations were then employed to fully understand the re-crystallization mechanism by which form I appears. Theory suggests that the serial route ($A \rightarrow II \rightarrow I$) should

involve a strong spatial correlation between form II and form I, and a strong anti-correlation between amorphous and form I.⁴⁶ The parallel route ($A \rightarrow II$ and $A \rightarrow I$) is expected to be random nucleation and growth of both forms II and I from amorphous. Each nearest “tablet” neighbor pixel to each “tablet” pixel has been classified (A/II/I) and counted as a function of time, so that transformations in polymorph can be monitored. To model the parallel route (random nucleation of forms I and II) a similar analysis was performed, differing only in that the neighboring pixels were replaced one-for-one by pixels selected randomly from across the compact (excluding the specific pixel of interest) at the relevant time point. The number of pixels with neighbors of which sort they are (A/II/I) at each time point is presented in Figure 7. The experimentally determined number of neighbors of each type is in good agreement with the modeled “random nucleation”, i.e., in accord with a predominantly parallel crystallization mechanism ($A \rightarrow II$ and $A \rightarrow I$ rather than $A \rightarrow II \rightarrow I$).

To summarize, both kinetic modeling of the classification data and detailed spatial analysis point toward the predominance of a non-Ostwald “parallel” crystallization mechanism, in which crystalline form I bicalutamide nucleates directly from the amorphous extrudate rather than from form II. Given that the amount of form II decreases after 889 min the pathway $II \rightarrow I$ clearly has some importance, but the main route for formation of form I appears to be direct random nucleation from the amorphous extrudate.

4. CONCLUSIONS

We have employed optical observation, rotating disc dissolution rate, and real-time Raman mapping to investigate the dissolution of bicalutamide:copovidone compacts for 5% and 50% drug loadings. The 5% sample dissolution mechanism involves the hydrophilic polymer and the hydrophobic drug

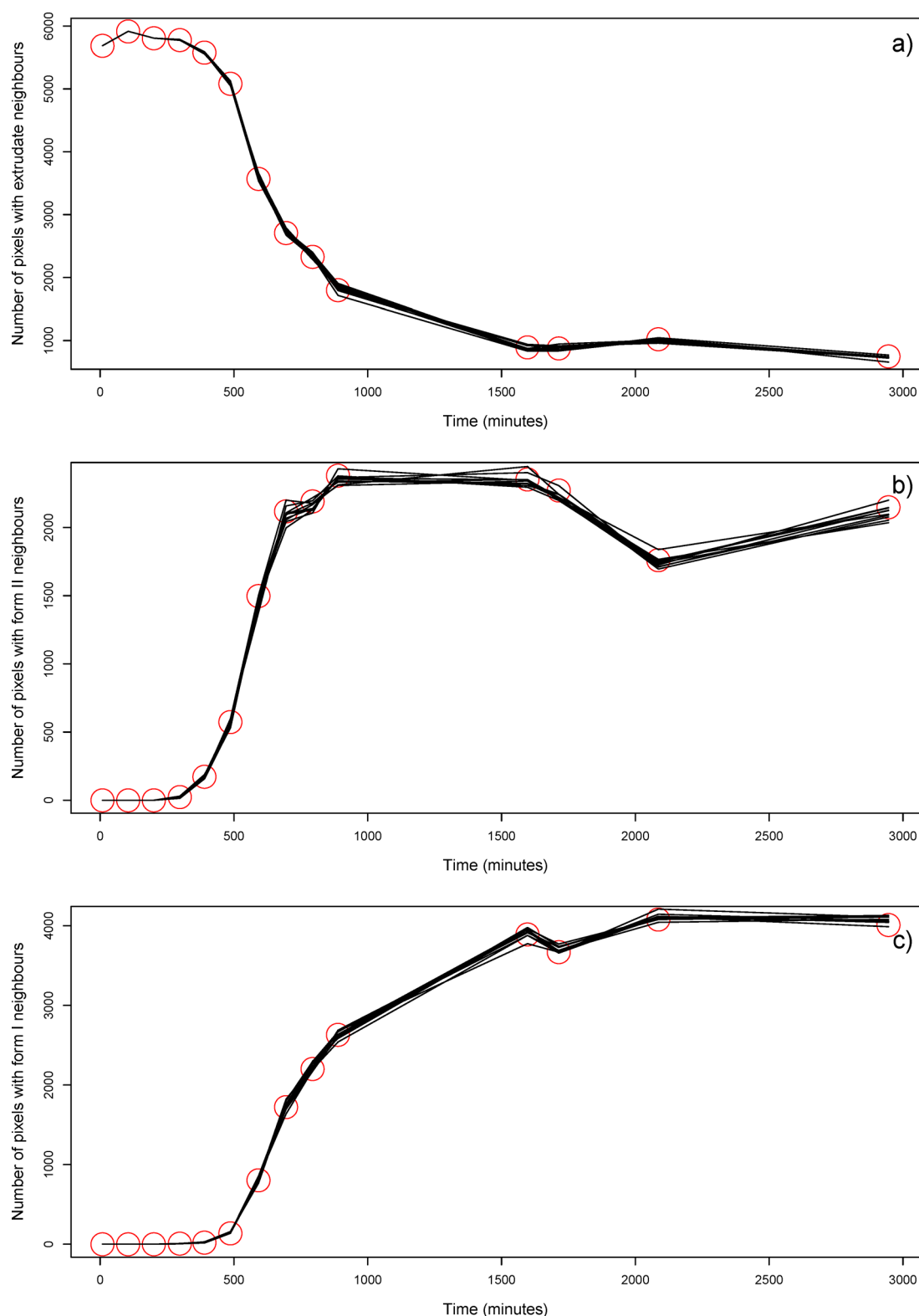


Figure 7. Spatial correlations between the “tablet” pixels and (a) amorphous, (b) form II, and (c) form I neighbors. The red circles indicate the experimental data, the black lines a set of 10 analyses in which neighbor spectra are replaced one-for-one by randomly selected pixels from that time map.

dissolving at the same rate, and the compact is completely dissolved after 85 min. In contrast, the 50% sample remains intact even after 3000 min. This is shown to be due to preferential dissolution of the hydrophilic polymer, which, we hypothesize, leads to a shell of amorphous hydrophobic drug

around the exterior of the compact. Our data indicate that this shell transforms first to metastable crystalline form II and then stable form I. Form I crystallizes preferentially from the amorphous form in a random nucleation mechanism, rather than from the crystalline form II. The interior of the compact is

protected from water ingress by the shell of hydrophobic drug and remains a copovidone:bicalutamide molecular dispersion, even after ca. 50 h immersion in flowing water. The dissolution behavior observed here and the hypothesized water-resistant “hydrophobic shell” of drug are likely to have significant implications for drug delivery and bioavailability optimization, and are likely to apply to a wide range of molecular dispersion formulations.

■ ASSOCIATED CONTENT

■ Supporting Information

Example of a thresholded image, kinetic trend showing how the surface area of the 50% extrudate changes during dissolution, RDDR and IDR trends, schematic of the structural conformations of forms I and II, averaged spectra of the dissolution of the 5% extrudate, remaining time-point maps of the 50% extrudate, XRPD data, kinetic model obtained by constraining the rate constant for $A \rightarrow I$ to be 0 min^{-1} , and raw data and numerical routines. This material is available free of charge via the Internet at <http://pubs.acs.org>.

■ AUTHOR INFORMATION

Corresponding Authors

*Phone: +44 (0) 1158468357. Fax: +44 (0) 1159515102. E-mail: francesco.tres@nottingham.ac.uk.

*E-mail: jonathan.burley@nottingham.ac.uk.

Notes

The authors declare no competing financial interest.

■ ACKNOWLEDGMENTS

Support from AstraZeneca and EPSRC through grant EP/I01375X/1 (via the joint Centre for Doctoral Training in Targeted Therapeutics and Formulation Sciences) is kindly acknowledged. We also thank the Nottingham Nanotechnology and Nanoscience Centre for the access to the Raman system.

■ REFERENCES

- (1) Babu, N. J.; Nangia, A. Solubility Advantage of Amorphous Drugs and Pharmaceutical Cocrystals. *Cryst. Growth Des.* **2011**, *11*, 2662–2679.
- (2) Hancock, B. C.; Parks, M. What is the True Solubility Advantage for Amorphous Pharmaceuticals? *Pharm. Res.* **2000**, *17*, 397–404.
- (3) Hancock, B. C.; Zografi, G. Characteristics and significance of the amorphous state in pharmaceutical systems. *J. Pharm. Sci.* **1997**, *86*, 1–12.
- (4) Murdande, S. B.; Pikal, M. J.; Shanker, R. M.; Bogner, R. H. Solubility advantage of amorphous pharmaceuticals: I. A thermodynamic analysis. *J. Pharm. Sci.* **2010**, *99*, 1254–1264.
- (5) Greenhalgh, D. J.; Williams, A. C.; Timmins, P.; York, P. Solubility parameters as predictors of miscibility in solid dispersions. *J. Pharm. Sci.* **1999**, *88*, 1182–1190.
- (6) Marsac, P. J.; Shamblin, S. L.; Taylor, L. S. Theoretical and Practical Approaches for Prediction of Drug–Polymer Miscibility and Solubility. *Pharm. Res.* **2006**, *23*, 2417–2426.
- (7) Leuner, C.; Dressman, J. Improving drug solubility for oral delivery using solid dispersions. *Eur. J. Pharm. Biopharm.* **2000**, *50*, 47–60.
- (8) Serajuddin, A. T. M. Solid dispersion of poorly water-soluble drugs: Early promises, subsequent problems, and recent breakthroughs. *J. Pharm. Sci.* **1999**, *88*, 1058–1066.
- (9) Yang, J.; Grey, K.; Doney, J. An improved kinetics approach to describe the physical stability of amorphous solid dispersions. *Int. J. Pharm.* **2010**, *384*, 24–31.
- (10) Ivanisevic, I. Physical stability studies of miscible amorphous solid dispersions. *J. Pharm. Sci.* **2010**, *99*, 4005–4012.
- (11) Langham, Z. A.; Booth, J.; Hughes, L. P.; Reynolds, G. K.; Wren, S. A. C. Mechanistic insights into the dissolution of spray-dried amorphous solid dispersions. *J. Pharm. Sci.* **2012**, *101*, 2798–2810.
- (12) Tres, F.; Treacher, K.; Booth, J.; Hughes, L. P.; Wren, S. A. C.; Aylott, J. W.; Burley, J. C. Real time Raman imaging to understand dissolution performance of amorphous solid dispersions. *J. Controlled Release* **2014**, *188*, 53–60.
- (13) Craig, D. Q. M. The mechanisms of drug release from solid dispersions in water-soluble polymers. *Int. J. Pharm.* **2002**, *231*, 131–144.
- (14) Alonzo, D. E.; Zhang, G. G. Z.; Zhou, D.; Gao, Y.; Taylor, L. S. Understanding the Behavior of Amorphous Pharmaceutical Systems during Dissolution. *Pharm. Res.* **2010**, *27*, 608–618.
- (15) Tho, I.; Liepold, B.; Rosenberg, J.; Maegerlein, M.; Brandl, M.; Fricker, G. Formation of nano/micro-dispersions with improved dissolution properties upon dispersion of ritonavir melt extrudate in aqueous media. *Eur. J. Pharm. Sci.* **2010**, *40*, 25–32.
- (16) Karavas, E.; Ktistis, G.; Xenakis, A.; Georgarakis, E. Effect of hydrogen bonding interactions on the release mechanism of felodipine from nanodispersions with polyvinylpyrrolidone. *Eur. J. Pharm. Biopharm.* **2006**, *63*, 103–114.
- (17) Gray, V.; Kelly, G.; Xia, M.; Butler, C.; Thomas, S.; Mayock, S. The Science of USP 1 and 2 Dissolution: Present Challenges and Future Relevance. *Pharm. Res.* **2009**, *26*, 1289–1302.
- (18) Pygall, S. R.; Whetstone, J.; Timmins, P.; Melia, C. D. Pharmaceutical applications of confocal laser scanning microscopy: The physical characterisation of pharmaceutical systems. *Adv. Drug Delivery Rev.* **2007**, *59*, 1434–1452.
- (19) van der Weerd, J.; Kazarian, S. G. Release of poorly soluble drugs from HPMC tablets studied by FTIR imaging and flow-through dissolution tests. *J. Pharm. Sci.* **2005**, *94*, 2096–2109.
- (20) Wray, P. S.; Clarke, G. S.; Kazarian, S. G. Dissolution of tablet-in-tablet formulations studied with ATR-FTIR spectroscopic imaging. *Eur. J. Pharm. Sci.* **2013**, *48*, 748–757.
- (21) Avale, P.; Pygall, S. R.; Gower, N.; Midwinter, A. The use of in situ near infrared spectroscopy to provide mechanistic insights into gel layer development in HPMC hydrophilic matrices. *Eur. J. Pharm. Sci.* **2011**, *43*, 400–408.
- (22) Avale, P.; Pygall, S. R.; Pritchard, J.; Jastrzemska, A. Interrogating erosion-based drug liberation phenomena from hydrophilic matrices using near infrared (NIR) spectroscopy. *Eur. J. Pharm. Sci.* **2013**, *48*, 72–79.
- (23) Chen, Y. Y.; Hughes, L. P.; Gladden, L. F.; Mantle, M. D. Quantitative ultra-fast MRI of HPMC swelling and dissolution. *J. Pharm. Sci.* **2010**, *99*, 3462–3472.
- (24) Richardson, J. C.; Bowtell, R. W.; Mäder, K.; Melia, C. D. Pharmaceutical applications of magnetic resonance imaging (MRI). *Adv. Drug Delivery Rev.* **2005**, *57*, 1191–1209.
- (25) Chan, K. L. A.; Kazarian, S. G. FTIR Spectroscopic Imaging of Dissolution of a Solid Dispersion of Nifedipine in Poly(ethylene glycol). *Mol. Pharmaceutics* **2004**, *1*, 331–335.
- (26) Windbergs, M.; Haaser, M.; McGoverin, C. M.; Gordon, K. C.; Kleinebudde, P.; Strachan, C. J. Investigating the relationship between drug distribution in solid lipid matrices and dissolution behaviour using Raman spectroscopy and mapping. *J. Pharm. Sci.* **2010**, *99*, 1464–1475.
- (27) Haaser, M.; Windbergs, M.; McGoverin, C. M.; Kleinebudde, P.; Rades, T.; Gordon, K. C.; Strachan, C. J. Analysis of matrix dosage forms during dissolution testing using Raman microscopy. *J. Pharm. Sci.* **2011**, *100*, 4452–4459.
- (28) Fussell, A.; Garbacik, E.; Offerhaus, H.; Kleinebudde, P.; Strachan, C. In situ dissolution analysis using coherent anti-Stokes Raman scattering (CARS) and hyperspectral CARS microscopy. *Eur. J. Pharm. Biopharm.* **2013**, *85*, 1141–1147.
- (29) Brillante, A.; Bilotti, I.; della Valle, R. G.; Venuti, E.; Girlando, A. Probing polymorphs of organic semiconductors by lattice phonon Raman microscopy. *CrystEngComm* **2008**, *10*, 937–946.
- (30) Al-Dulaimi, S.; Aina, A.; Burley, J. C. Rapid polymorph screening on milligram quantities of pharmaceutical material using

phonon-mode Raman spectroscopy. *CrystEngComm* **2010**, *12*, 1038–1040.

(31) Abu-Diak, O. A.; Jones, D. S.; Andrews, G. P. Understanding the performance of melt-extruded poly(ethylene oxide)–bicalutamide solid dispersions: Characterisation of microstructural properties using thermal, spectroscopic and drug release methods. *J. Pharm. Sci.* **2012**, *101*, 200–213.

(32) Andrews, G. P.; AbuDiak, O. A.; Jones, D. S. Physicochemical characterization of hot melt extruded bicalutamide–polyvinylpyrrolidone solid dispersions. *J. Pharm. Sci.* **2010**, *99*, 1322–1335.

(33) Németh, Z.; Sztatisz, J.; Demeter, A. Polymorph transitions of bicalutamide: A remarkable example of mechanical activation. *J. Pharm. Sci.* **2008**, *97*, 3222–3232.

(34) Vega, D. R.; Polla, G.; Martinez, A.; Mendioroz, E.; Reinoso, M. Conformational polymorphism in bicalutamide. *Int. J. Pharm.* **2007**, *328*, 112–118.

(35) Breitenbach, J. Melt extrusion can bring new benefits to HIV therapy. *Am. J. Drug Delivery* **2006**, *4*, 61–64.

(36) *United States Pharmacopoeia 31 and National Formulary 26*; The United States Pharmacopeial Convention, Inc.: Rockville, Md, 2008.

(37) Westheim, R. Bicalutamide forms. U.S. Patent 20040063782, 2004.

(38) *European Pharmacopoeia*, 6th ed.; Directorate for the Quality of Medicines and Healthcare of the Council of Europe: Strasbourg, France, 2008.

(39) R Development Core Team. *R: A language and environment for statistical computing*; R Foundation for Statistical Computing: Vienna, Austria, 2011.

(40) Gendrin, C.; Roggo, Y.; Collet, C. Pharmaceutical applications of vibrational chemical imaging and chemometrics: A review. *J. Pharm. Biomed. Anal.* **2008**, *48*, 533–553.

(41) Gallagher, N. B.; Shaver, J. M.; Martin, E. B.; Morris, J.; Wise, B. M.; Windig, W. Curve resolution for multivariate images with applications to TOF-SIMS and Raman. *Chemometr. Intell. Lab. Syst.* **2004**, *73*, 105–117.

(42) Duponchel, L.; Elmi-Rayaleh, W.; Ruckebusch, C.; Huvenne, J. P. Multivariate Curve Resolution Methods in Imaging Spectroscopy: Influence of Extraction Methods and Instrumental Perturbations. *J. Chem. Inf. Comput. Sci.* **2003**, *43*, 2057–2067.

(43) Awa, K.; Okumura, T.; Shinzawa, H.; Otsuka, M.; Ozaki, Y. Self-modeling curve resolution (SMCR) analysis of near-infrared (NIR) imaging data of pharmaceutical tablets. *Anal. Chim. Acta* **2008**, *619*, 81–86.

(44) Rutan, S.; de Juan, A.; Tauler, R. Introduction to Multivariate Curve Resolution. *Comprehensive Chemometrics*; Elsevier: Oxford, 2009; Vol. 2, Chapter 2.15, pp 249–259.

(45) de Juan, A.; Rutan, S.; Tauler, R. Two-Way Data Analysis: Multivariate Curve Resolution—Iterative Resolution Methods. *Comprehensive Chemometrics*; Elsevier: Oxford, 2009; Vol. 2, Chapter 2.19, pp 325–344.

(46) Snyder, V.; Alkemper, J.; Voorhees, P. The development of spatial correlations during Ostwald ripening: a test of theory. *Acta Mater.* **2000**, *48*, 2689–2701.